

Article

Parameter optimization of membrane mlectrode assembly in Fuel Cell based on improved differential evolution algorithm: biomechanical stress and strain considerations

Ting Lu, Yan Liu*

Key Laboratory of Bionic Engineering (Ministry of Education), College of Bionic Science and Engineering, Jilin University, Changchun 130022, China

* **Corresponding author:** Yan Liu, jlul22@163.com

CITATION

Lu T, Liu Y. Parameter optimization of membrane mlectrode assembly in Fuel Cell based on improved differential evolution algorithm: biomechanical stress and strain considerations. *Molecular & Cellular Biomechanics*. 2025; 22(2): 1035. <https://doi.org/10.62617/mcb1035>

ARTICLE INFO

Received: 7 December 2024
Accepted: 12 December 2024
Available online: 22 January 2025

COPYRIGHT



Copyright © 2025 by author(s).
Molecular & Cellular Biomechanics
is published by Sin-Chn Scientific
Press Pte. Ltd. This work is licensed
under the Creative Commons
Attribution (CC BY) license.
<https://creativecommons.org/licenses/by/4.0/>

Abstract: The membrane electrode assembly in a proton exchange membrane fuel cell (PEMFC) functions as the electrochemical reaction region, where the generated electric current relies on the diffusion of reactant gases and electron conduction. Drawing inspiration from biomechanics, this study embarked on constructing a database of PEMFC performance data. Similar to how biomechanical studies use advanced imaging and sensing techniques to map the internal workings of organisms, three-dimensional computational fluid dynamics (CFD) simulations were employed to capture the intricate fluid and gas behaviors within the fuel cell. The data was then used to train data-driven surrogate models based on artificial neural network (ANN) and improved differential evolution for rapid prediction and optimization. When considering the biomechanical aspects, we analyze the mechanical stresses and strains that occur within the membrane electrode assembly during operation. These biomechanical factors can affect the durability and performance of the fuel cell. The gas diffusion layer (GDL) is similar to the pore structure in biological tissues. The pore structure of biological organisms, such as bones, not only ensures the diffusion and transport of nutrients, but also provides space for the attachment of cells to maintain the growth and metabolism of bones. The optimization results revealed that the pores of the GDL, just like the pores of biological tissues, affect the diffusion efficiency of the reactant gases (similar to nutrients) to the catalytic layer, and an appropriate porosity ensures the supply of the reactants required for the electrochemical reactions inside the cell, and improves the PEMFC performance of the cell. By utilizing the random forest algorithm (RF) to conduct feature importance evaluation, we can gain further understanding and interpretation of the factors influencing coupling relationships. The researchers successfully identified the optimal values of GDL porosity and thickness, resulting in an 8.75% increase in power density and significant improvement in oxygen distribution uniformity. To validate the effectiveness and accuracy of the optimization, the optimized structural parameters were incorporated into CFD simulations. The validation results demonstrated close alignment between the optimized model's performance and actual values, confirming the efficacy and reliability of the optimization framework. Overall, this data-driven optimization approach provides an effective tool for multi-variable optimization of complex systems and holds significant importance in enhancing the performance and power density of PEMFC, while also taking into account the biomechanical factors that influence its long-term operation and stability.

Keywords: membrane electrode assembly; parameter optimization; artificial neural network; random forest algorithm; differential evolution; biomechanical stresses

1. Introduction

In recent years, the demand for new energy sources in the market has intensified due to energy shortages and environmental pollution [1]. Hydrogen has emerged as a clean and efficient energy source, garnering global attention for its development. One such technology is proton exchange membrane fuel cell (PEMFC) [2], an electrochemical apparatus that directly transforms the chemical power of a fuel into electricity. PEMFC offers several advantages including high efficiency, durability, light weight, fast start-up, and environmental friendliness. It has found applications in stationary power sources, portable power sources, and electric vehicles. However, before achieving large-scale commercialization, there is a need for improvements in the power density, cost, lifetime, and durability performance of PEMFC [3].

The membrane electrode assembly (MEA) serves as the core component of PEMFCs and plays a critical role in battery life, performance, and cost. Two important components of the MEA, the gas permeation layer (GDL) and the reaction-catalyzing layer (CL), have attracted significant attention from researchers. The GDL has multiple functions, including uniform transportation of reactants to the reaction zone and providing drainage channels. Several factors affect its performance, for instance, characteristics like pore volume fraction, gas transmission capability, electrical conductance, interfacial resistance, and dimensional thickness. To study the transport phenomena in GDL more comprehensively, scientists have crafted diverse GDL (Gas Diffusion Layer) representations, which can be grouped into two primary classes: uniform porosity models and non-uniform porosity models. In the case of homogeneous modeling, Turkmen and Celik [4] improved PEMFC performance by optimizing the porosity of the GDL. They analyzed cell performance at different porosities and found that a porosity of 0.6 yielded the most significant improvement in cell performance at high current densities. On the other hand, Yang et al. [5] established a non-uniform porosity model for the GDL and enhanced battery performance. They observed that changes in porosity had a substantial impact on cell performance, particularly at high current densities, and increasing the porosity of the GDL cathode improved current density and water distribution uniformity. Regarding the catalytic layer, one of its functions is to catalyze electrochemical reactions, facilitate proton and electron transport, and transfer product water to the GDL. Researchers have investigated the effect of CL composition on its performance. For instance, Wang et al. [6] achieved higher power density by optimizing the platinum (Pt) catalyst content and the ratio of carbon carrier to ionomer in the CL. They found that an optimal ratio, obtained through an artificial intelligence approach combined with experimental data, led to a maximum power density of 1.2473 W/cm². Deng et al. [7] analyzed the impact of CL microstructure on PEMFC performance. They discovered that increasing the ionomer content and Pt loading improved the electrochemical reaction rate. However, due to small porosity, reactant transport became more challenging, resulting in inefficient participation of the Pt catalyst in some regions and wasted catalyst material. Liu et al. [8] enhanced the PEMFC's output by adjusting the porosity of the catalytic layer (CL), the proportion of electrolyte, and the porosity of the gas diffusion layer (GDL), while simultaneously

decreasing the power density related to the electrolyte volume fraction. The optimized configuration featured a CL porosity of 0.2647, an electrolyte proportion of 0.4471, and a GDL porosity of 0.5043, achieved a 3.56% increase in maximum output power density and a 10.58% reduction in electrolyte volume fraction compared to the original model. Many prior investigations have concentrated solely on either the gas diffusion layer (GDL) or the catalytic layer (CL), neglecting their combined impact. However, considering the combined effect of both components will lead to better overall performance improvements in PEMFC.

Artificial intelligence (AI) methods are extensively employed in scientific research and engineering applications to address practical problems [9]. In the pursuit of improving fuel cell performance and optimizing time efficiency, many researchers have integrated AI methods for analysis. For instance, Li et al. [10] introduced a system that integrates advanced metaheuristic algorithms with machine learning techniques for predicting performance and optimizing parameters of proton exchange membrane fuel cells. They acquired a database through simulations and experiments, developed a prediction model based on an extreme learning machine, and used this model as a proxy to enhance the Gray Wolf optimizer. This methodology allowed them to achieve the best mix of structural and operational variables to enhance power density to its maximum. Liu et al. [8] focused on analyzing the impact of gradient porosity, thickness, the influence of operating voltage and pressure on proton exchange membrane fuel cells. They identified a consistency issue in numerous studies regarding the enhancement of fuel cell performance and extension of its lifetime. To tackle this issue, they developed a neural network model utilizing a substantial dataset and introduced a multi-objective genetic optimization algorithm grounded in a reconciliation strategy for optimization. Their algorithm was designed to enhance the uniformity of power output and oxygen molar concentration distribution in fuel cells [11]. The outcomes of the optimization showed a 1.45% boost in fuel cell efficiency and a 10.28% improvement in the uniformity of oxygen distribution, leading to more uniform oxygen distribution and an extended fuel cell lifetime. Huo et al. [12] employs deep learning techniques to devise an RF (Random Forest) methodology that incorporates the random forest algorithm alongside convolutional neural networks, which can reduce the dimension of input parameters to save computational resources and unnecessary experiments for MEA development.

The joint effect of GDL thickness, cathode porosity, and CL porosity has not been previously studied [13]. The importance of the parameters calculated by the RF and analysis of parameter selection and optimization. These parameters are associated with different structures, reactants, and transfer mechanisms. The gas travels through the GDL to reach the CL, and product water from the CL needs to be transferred via the GDL [14]. Consequently, there exists a coupling relationship among these parameters. To effectively deal with the nonlinear functions and capture the complex relationships, a neural network algorithm is employed. This algorithm utilizes historical input-output data to establish a mapping between the output and input variables. It can accurately predict the relationship between multiple variables and the desired output targets. In this paper, the authors initially set up a three-dimensional, steady-state Computational Fluid Dynamics (CFD) model of a Proton Exchange Membrane Fuel Cell (PEMFC) to serve as the foundation for optimization [15]. The model's

accuracy is verified through experimental data. Subsequently, a surrogate model is constructed using an artificial neural network. Finally, the surrogate model is combined with an improved differential evolution algorithm based on artificial neural network for parameter optimization. When compared to the baseline model, the optimized version exhibits enhancements in power density, reactant distribution, and pressure drop across all these dimensions.

2. PEMFC simulation model

2.1. Geometric model

The computational region for the PEMFC (Proton Exchange Membrane Fuel Cell) model is defined. This PEMFC model comprises two current collectors, two gas distribution plates, two gas diffusion layers (GDLs), two catalytic layers (CLs) on both cathode and anode sides, and a membrane electrode assembly (MEM). **Figure 1** illustrates the geometric configuration of the PEMFC model. **Table 1** lists the geometric parameters and **Table 2** shows the operating conditions of the PEMFC model. Due to the intricacy of the PEMFC system, the following assumptions of the numerical simulation was conducted based on [16]:

- (1) The PEMFC system operates under stable, constant conditions.
- (2) Gas flow within the PEMFC is considered perfect and non-compressible.
- (3) The PEMFC maintains a uniform temperature during operation.
- (4) The membrane electrode assembly is presumed to be uniform and consistent in all directions.

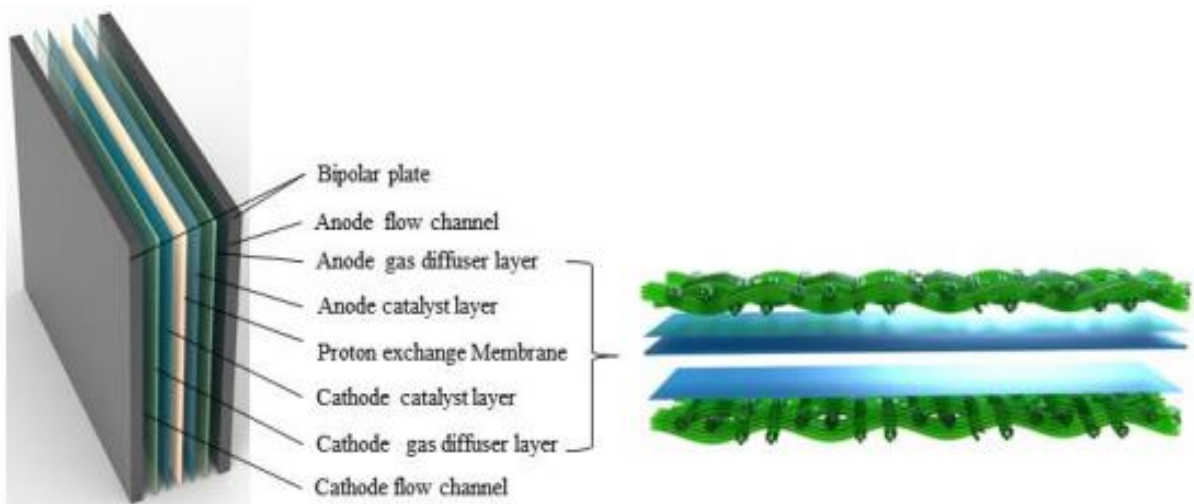


Figure 1. Schematic diagram of PEMFC model with parallel flow field.

Table 1. Geometric parameters of PEMFC model.

Parameters	Value	Unit
BPP length	50	mm
BPP width	50	mm
BPP height	2.0	mm
Flow field height	1.0	mm
Flow field width	1.0	mm

Table 1. (Continued).

Parameters	Value	Unit
Rib width	1.0	mm
GDL thickness	0.2	mm
CL thickness	0.0129	mm
MEM thickness	0.108	mm
Active area	2500	mm ²

Table 2. Operating conditions of PEMFC model.

Parameter	Unit	Value
Operation temperature	K	353.15
Operation pressure	Pa	101,325
Open-circuit voltage	V	0.98
Anode reference current density	A/m ²	20,000
Cathode reference current density	A/cm ²	0.5
Relative Humidity	-	100%
Anodic stoichiometry ratio	-	1.5
Cathode stoichiometry ratio	-	2
Reference hydrogen concentration	mol/m ³	56.4
Reference oxygen concentration	mol/m ³	3.39
Anode exchange coefficient	-	1
Cathode exchange coefficient	-	1
Anode concentration exponent	-	0.5
Cathode concentration exponent	-	1
Contact resistivity	Ω -m ²	1.50 ⁻⁶
H ₂ reference diffusivity	m ² /s	1.1 × 10 ⁻⁴
O ₂ reference diffusivity	m ² /s	3.2 × 10 ⁻⁵
H ₂ O reference diffusivity	m ² /s	7.35 × 10 ⁻⁵
Other species reference diffusivity	m ² /s	1.1 × 10 ⁻⁵
GDL porosity	-	0.7
CL porosity	-	0.2
Membrane porosity	-	0.25
Faraday's constant	C/mol	96,487
Universal gas constant	J/mol K	8.314

2.2. Governing equations

The numerical PEMFC model integrates several equations, such as those for continuity, momentum, energy, species conservation, charge conservation, and liquid water generation and transport [17]. Additionally, an equation linking porosity and diffusion flux, derived from Fick's [18] law, is included. **Table 3** presents the conservation equations for the fuel cell model, while **Table 4** lists the source terms involved in these equations [19]. Here's a concise summary of the main governing equations:

Table 3. Fuel cell model conservation equations.

Conservation equations	Equations
Continuity equation:	$\frac{\partial(\varepsilon\rho)}{\partial t} + \nabla \cdot (\varepsilon\rho\vec{v}) = S_m$
Momentum	$\frac{\partial(\varepsilon\rho\vec{v})}{\partial t} + \nabla \cdot (\varepsilon\rho\vec{v}\vec{v}) = -\varepsilon\nabla p + \nabla \cdot (\varepsilon\mu\nabla\vec{v}) + S_v$
Energy	$\frac{\partial(\varepsilon\rho c_p T)}{\partial t} + \nabla \cdot (\varepsilon\rho c_p \vec{v}T) = \nabla \cdot (k_{eff}\nabla T) + S_Q$
Species diffusion	$\frac{\partial(\varepsilon c_k)}{\partial t} + \nabla \cdot (\varepsilon c_k \vec{v}) = \nabla \cdot (D_k^{eff}\nabla c_k) + S_k$
Charge conservation	$\nabla \cdot (\sigma_s \nabla \phi_s) + S_{\phi_s} = 0$ $\nabla \cdot (\sigma_m \nabla \phi_m) + S_{\phi_m} = 0$
porosity and diffusion flux	$J = -D \frac{\partial C}{\partial z}$

Table 4. Source terms in the equations.

Source terms	Equations
S_m	$ACL: S_m = S_{H_2} = -\frac{M_{H_2}}{2F} R_a$ $CCL: S_m = S_{H_2O} + S_{O_2} = \frac{M_{H_2O}}{2F} i_c - \frac{M_{O_2}}{4F} R_c$
S_v	$\frac{\partial(\varepsilon\rho\vec{v})}{\partial t} + \nabla \cdot (\varepsilon\rho\vec{v}\vec{v}) = -\varepsilon\nabla p + \nabla \cdot (\varepsilon\mu\nabla\vec{v}) + S_v$
S_Q	$S_Q = (i^s)^2 R_{ohm} + \beta S_{H_2O} h_{rea} + r_w h_a, c_{lg}$
S_k	$\frac{\partial(\varepsilon c_k)}{\partial t} + \nabla \cdot (\varepsilon c_k \vec{v}) = \nabla \cdot (D_k^{eff}\nabla c_k) + S_k$
$S_{H_2} S_{O_2} S_{H_2O}$	$S_{H_2} = -\frac{1}{2F} R_a \quad S_{O_2} = -\frac{1}{4F} R_c \quad S_{H_2O} = \frac{1}{2F} R_c$
S_a	$S_a = (\zeta_a j_{a,ref}) \left(\frac{C_{H_2}}{C_{H_2,ref}} \right)^{\gamma_a} \left(e^{\frac{\alpha_a F}{RT} \eta_a} - e^{-\frac{\alpha_c F}{RT} \eta_a} \right)$
S_c	$S_c = (\zeta_c j_{c,ref}) \left(\frac{C_{O_2}}{C_{O_2,ref}} \right)^{\gamma_c} \left(e^{\frac{\alpha_c F}{RT} \eta_c} - e^{-\frac{\alpha_a F}{RT} \eta_c} \right)$
σ	$GDL: \sigma = (1 - \varepsilon)^{1.5} \cdot \sigma_0$ $CL: \sigma = (1 - \varepsilon - \omega)^{1.5} \cdot \sigma_0$

2.3. Boundary conditions

The boundary conditions for the PEMFC zones have been specified. The mass flow rate (in kg per second) at the inlets of both the anode and cathode flow fields can be determined using the following formula:

$$m_{in,a} = \frac{\rho_a \xi_a i_{ref} A}{2F} \frac{RT}{P_{inlet,a} - RH_a P_{sat}} \quad (1)$$

$$m_{in,c} = \frac{\rho_c \xi_c i_{ref} A}{4F} \frac{RT}{0.21(P_{inlet,c} - RH_c P_{sat})} \quad (2)$$

where ρ_a and ρ_c , ξ_a and ξ_c and $P_{inlet,a}$ and $P_{inlet,c}$ represent density of the gas mixed density, stoichiometry flow ratio and inlet pressure of the anode and cathode. A represents the active in CL; the reference current density is denoted as i_{ref} ; and RH_a

and RH_c are the hydrogen and air relative humidities. These parameters can be sourced from Hu et al. [20].

2.4. Model validation

To ensure the precision and dependability of the numerical solution results, five distinct levels of mesh refinement (specifically, 440,235 elements, 771,259 elements, 1,046,659 elements, 1,353,327 elements, and 2,035,685 elements) were tested to validate grid independence. The PEMFC's current density was calculated using these various meshes at a cell operating voltage of 0.5 V. As illustrated in **Figure 2**, as the mesh density increases, the fuel cell's current density gradually rises. The relative error in current density between the meshes with 1,046,659 and 1,353,327 elements is less than 0.5%. Therefore, a mesh system with 1,353,327 elements was selected for all PEMFC simulations to balance accuracy and computational efficiency.

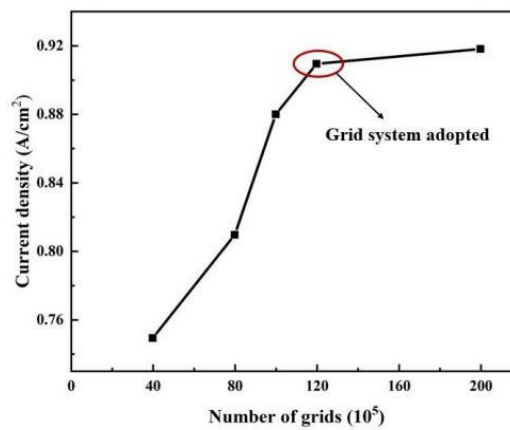


Figure 2. Grid independence test.

To confirm the PEMFC model's reliability, the numerical polarization curves were compared to the experimental data provided by Guo et al. [21] in Fig6. As depicted in **Figure 3**, the current density curves align well with the experimental data from previous studies. Furthermore, the maximum discrepancies between the results are less than 6.0% [22]. Consequently, the current model is deemed reasonable and suitable for predicting PEMFC polarization behavior, and it can be utilized for subsequent parameter optimization.

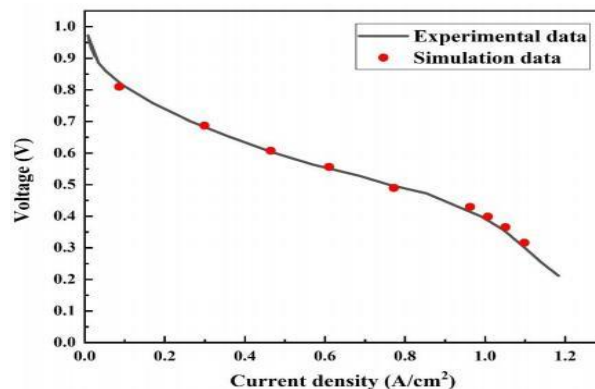


Figure 3. Comparison between the polarization curves based on the present model and the literature data.

3. Optimization process

3.1. Artificial neural networks

Artificial neural network (ANN) is a computational model inspired by the human nervous system, capable of simulating and solving complex nonlinear problems. It possesses self-learning capabilities, allowing it to make accurate predictions by processing large amounts of data. ANN consist of interconnected neurons that receive inputs, undergo certain processing, and produce outputs, influenced by adjustable weight parameters. They do not require knowledge of the exact input-output relationship but focus on the data itself [23]. Consequently, ANN offer advantages in adaptive learning, nonlinear modeling, and parallel computing compared to traditional data processing methods [24]. PEMFC, being complex systems with coupled mass transfer, energy, and electrochemical reactions, benefit from neural networks due to their inherent complexity. The thickness of the GDL, the porosity of the anode cathode GDL, and the porosity of the anode cathode CL are the main factors affecting the distribution of PEMFC reactants. Therefore, these five factors were selected as input variables in this study, and the selection range of input variables is shown in **Table 5**. Various research methods exist for neural networks, and in this study, ANNs are employed to process 243 data sets obtained from Ansys. The neural networks are trained using the TensorFlow library.

Inputs to the neural networks include gas diffusion layer porosity, gas diffusion layer thickness, and catalytic layer porosity, as shown in the **Figure 4** while the power density index serves as the output [25].

Table 5. Input parameter settings.

Parameters	Range of values	Units
GDL thickness	0.2, 0.3, 0.4	mm
GDL anode porosity	0.3, 0.5, 0.7	-
GDL cathode porosity	0.3, 0.5, 0.7	-
CL anode porosity	0.2, 0.35, 0.5	-
CL cathode porosity	0.2, 0.35, 0.5	-

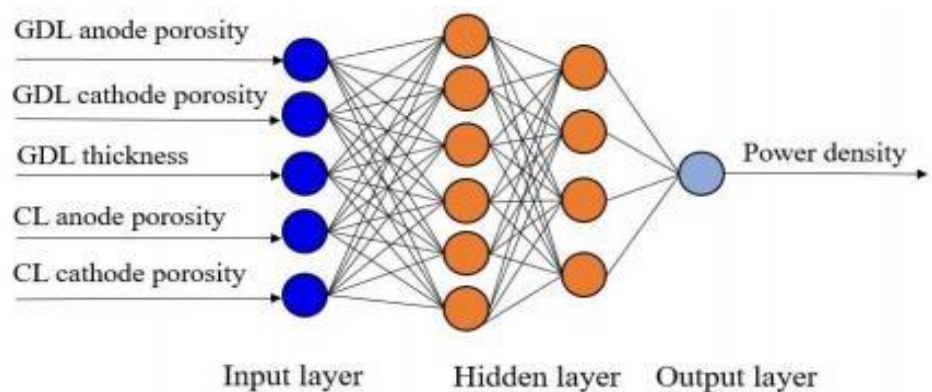


Figure 4. The topological structure of the ANN model.

3.2. Differential evolutionary algorithm

Differential evolution (DE) is a global optimization algorithm introduced by Rainer Storn and Kenneth Price, falling under the umbrella of evolutionary algorithms [26].

The differential evolution algorithm has the advantages of simplicity, efficiency and easy implementation, and it shows good performance in solving optimization problems. In practical applications, the differential evolutionary algorithm needs to be adjusted and improved according to specific problems, such as setting appropriate parameters, changing variation strategies, crossover strategies, etc., to enhance the algorithm's performance and the quality of the solution. Therefore, the differential evolution algorithm has gained broader application in tackling complex problems [27–29].

The steps of DE algorithm implementation are as follows:

The differential evolution algorithm uses a random function to generate the initial population to ensure that the population covers the entire search space. $X(G)$ denotes the population at the time of evolution to the G -th generation.

$$X_{i,j}^G = X_{i,j}^L + f \times (X_{i,j}^U - X_{i,j}^L) \quad (3)$$

The random function initializes the population as shown by Equation (3). where $X_{i,j}^G$ denotes the j -th component on the i -th individual of the G -th generation. $\text{Rand}(0, 1)$ means a random number between 0 and 1, $X_{i,j}^U$ and $X_{i,j}^L$ denote the lower and upper bounds of the solution, respectively.

$$V_i^{G+1} = X_{r_3}^G + F \times (X_{r_1}^G - X_{r_2}^G) \quad (4)$$

Two different individuals $X_{r_1}^G$ and $X_{r_2}^G$ are randomly generated from the G -th generation population, and then the vector difference is added to another randomly generated $X_{r_3}^G$ individual vector to generate the variant individuals.

$$U_{i,j}^{G+1} = V_{i,j}^{G+1} \quad \text{if } (f \leq CR \text{ or } j = \text{rand}(i)) \text{ else } X_{i,j}^G \quad (5)$$

where CR between 0 and 1, f is a random number between 0 and 1, and $\text{rand}(i)$ is a random number between 1 and D , and D is the dimension. This makes $U_{i,j}^G$ at least one component from $V_{i,j}^{G+1}$, and at least one component different from $X_{i,j}^G$.

$$X_{i+1,j}^G = U_{i,j}^G \quad \text{if } (F(U) > F(X)) \text{ else } X_{i,j}^G \quad (6)$$

The DE algorithm performs selection operations based on the principle of greedy preservation of superiority. It compares the fitness of the old and new individuals and leaves the better one. As shown in Equation (6).

3.3. Improved differential evolution algorithm

The improved differential evolution (IDE) algorithm is designed to address the effect of population diversity on the evolutionary algebra, balancing the global search and local search of the algorithm by redirecting the variation and crossover operations. Proposed positive and reverse learning factors are proposed to accelerate convergence rate [30–32]. The improved mathematical principles are introduced:

$$C_{1i,j}^{G+1} = X_{i,j}^G + f1 * (X_{best,j}^G - X_{i,j}^G) \quad \text{Positive Evolution} \quad (7)$$

$$C_{2i,j}^{G+1} = X_{i,j}^G + f2 * (X_{worst,j}^G - X_{i,j}^G) \quad \text{Reverse Evolution} \quad (8)$$

where $X_{i,j}^G$ denotes the j -th component on the i -th individual of the G -th generation, $X_{best,j}^G$ is the optimal value of the current population, $f1$ is the positive evolution factor with a value of 0.9, and $f2$ is the reverse evolution factor with a value of 0.1. During the variation, the positive learning of the globally optimal individual is achieved by learning from the individual with the best fitness value in the population in order to improve the search speed of the individual quickly, as shown in Equation (7). During the process of searching for the optimal solution, when there are multiple input variables, it is possible to encounter multiple local extremum points. This makes the algorithm prone to getting stuck in a local optimal solution, thus preventing it from converging quickly to the global optimal solution. When the global optimum individual remains unchanged after several iterations, individuals in the population learning process may learn from the worst individual. as shown in Equation (8), can make the algorithm jump out of the local extremes with a certain probability, expand the search space, and thus improve the convergence speed quickly.

3.4. Performance prediction process

3.4.1. Data pre-processing

The initial step in data preprocessing involves gathering raw data from the 3D simulation model and processing it. Additionally, the PEMFC's operating and geometric parameters, such as gas diffusion layer porosity, thickness, and catalytic layer porosity [24], are taken into account to ensure the reliability of the data. **Table 6** outlines the range of input parameters. By combining various parameters, the total number of raw data points utilized by the neural network amounts to 324 (calculated as $4 \times 3 \times 3 \times 3 \times 3$) [33].

Since the values of the input variables are not in the same order of magnitude, for example, the thickness varies between 0.1 and 0.3 while the porosity varies between 0.2 and 0.8, the training data must be preprocessed to scale the variables to the same range before training to accelerate the convergence of the neural network [34]. The following equation is used to scale all the original data to the [0, 1] range:

$$X = \frac{x - x_{\min}}{x_{\max} - x_{\min}} \quad (9)$$

3.4.2. Prediction and evaluation

The 324 datasets were randomly partitioned into a training set, a cross-validation set, and a test set in a 6:2:2 ratio, with the training set comprising 240 datasets and both the cross-validation and test sets containing 84 datasets each [35]. In mathematical statistics, the mean square error (MSE) represents the average of the squared differences between an estimator's value and the true value of a parameter. MSE serves as a practical metric for assessing mean error and evaluating data variability, where a lower MSE indicates a higher degree of accuracy in the

prediction model's description of experimental data. Both the mean square error (MSE) and the correlation coefficient (R_2) were employed as cost functions [36].

$$MSE = \frac{1}{n} \sum_{i=1}^n (f_i - y_i)^2 \quad (10)$$

$$R^2 = 1 - \frac{\sum_{i=1}^n (y_i - \hat{y})^2}{\sum_{i=1}^n (f_i - \bar{y})^2} \quad (11)$$

where n is the number of input samples; \hat{y} is the predicted value; y_i denotes the actual value; and \bar{y} is the average of y_i . During the final phase of development, the effectiveness of the proposed model is assessed. The model's output is contrasted with the test set data, and the prediction error is computed. A detailed discussion on the predicted outcomes is provided in the subsequent section.

3.5. Optimization framework based on the surrogate model

Figure 5 displays the flowchart of the proposed optimization framework, which integrates the data-driven model with the IDE algorithm. The ANN-based predictive model serves as an alternative for evaluating the objective function of the IDE algorithm. This optimization process does not rely on any assumptions, and the specific ranges for the optimization parameters are listed in **Table 6**. The maximum iteration count is set to 200, with a population size of 200. Once the IDE algorithm identifies the optimal parameters, the CFD model is utilized to further verify the optimization results obtained through the framework [37,38]. RF is a model composed of various decision trees. One of its functions is to analyze the importance of features [39]. By using the algorithm to determine their importance, we can reveal the relationships between the features. We can set the number of decision trees in the RF algorithm to 30, set the maximum depth of each tree to 5.

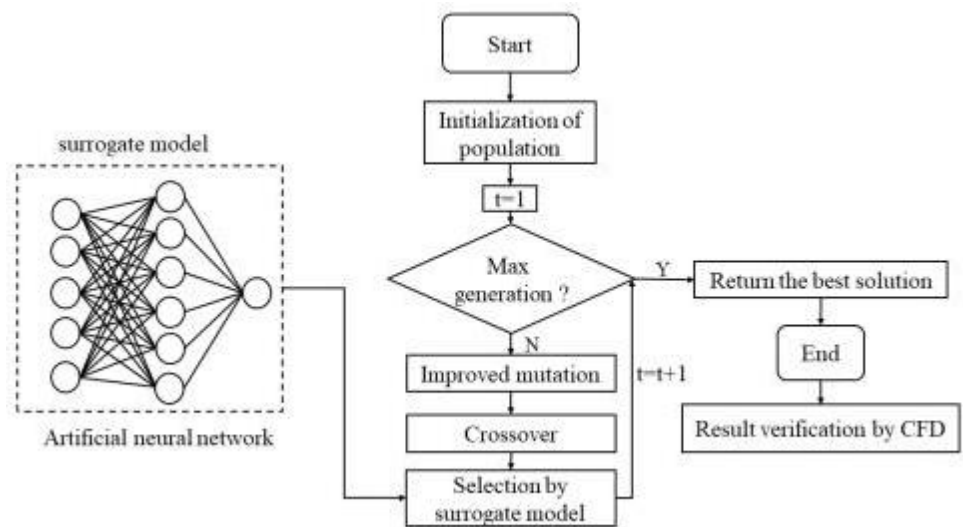


Figure 5. The flowchart of the framework based on the IDE algorithm.

Table 6. Specific range of optimization parameters.

Parameters	Min values	Max values
GDL thickness	0.2	0.4
GDL anode porosity	0.3	0.7
GDL cathode porosity	0.3	0.7
CL anode porosity	0.2	0.5
CL cathode porosity	0.2	0.5

4. Results and discussion

4.1. Predicted results

The predictive accuracy of the ANN model for current density was assessed. **Figure 6** presents a comparison of the predicted and measured current densities for the training, validation, and test sets of the simulated data. The R_2 values achieved for these sets are 0.9974, 0.986, and 0.989, respectively, suggesting a high degree of correlation between the predicted and actual values. Additionally, the maximum absolute error was found to be 0.00274, demonstrating a close match between the predicted and simulated values. In summary, the ANN model demonstrates excellent predictive accuracy, as the predicted values align well with the simulated values of the current density [40,41].

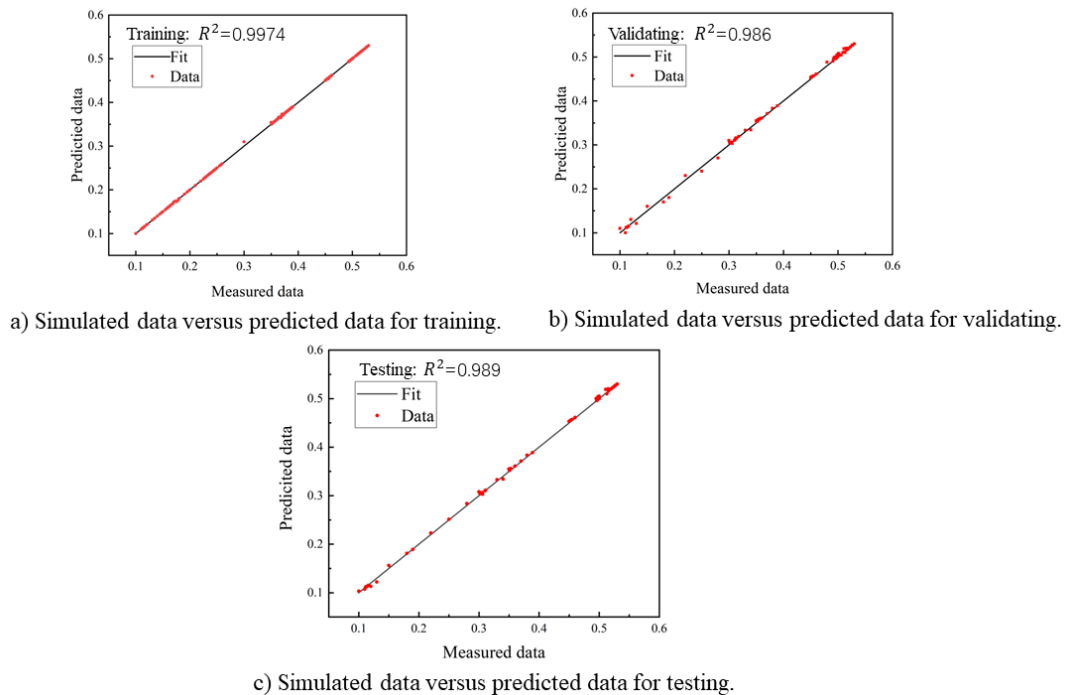


Figure 6. Correlation between measured and predicted points for (a) training, (b) validating, and (c) test set.

4.2. Effect of parameters on performance

4.2.1. Effect of GDL thickness on performance

The thickness of GDL is a crucial factor influencing the performance of PEMFCs. The **Figure 7** illustrates the current density for three different GDL thicknesses: 2 mm, 2.5 mm, 3 mm, 3.5 mm and 4 mm. It shows that the performance

of the PEMFC initially increases and then decreases as the GDL thickness varies. A thinner GDL tends to cause a non-uniform distribution of oxygen and liquid water within the fuel cell. This uneven distribution can lead to localized areas of high and low reactant concentrations, affecting the overall performance. On the other hand, a thicker GDL increases the resistance to oxygen transport, making it more challenging for the reactant gas to diffuse to the reaction surface. Consequently, this results in a decrease in the concentration of reactants in the CL. Therefore, there exists an optimum GDL thickness that strikes a balance between ensuring sufficient oxygen and water distribution while minimizing transport resistance. Deviating from this optimal thickness can negatively impact the performance of PEMFC.

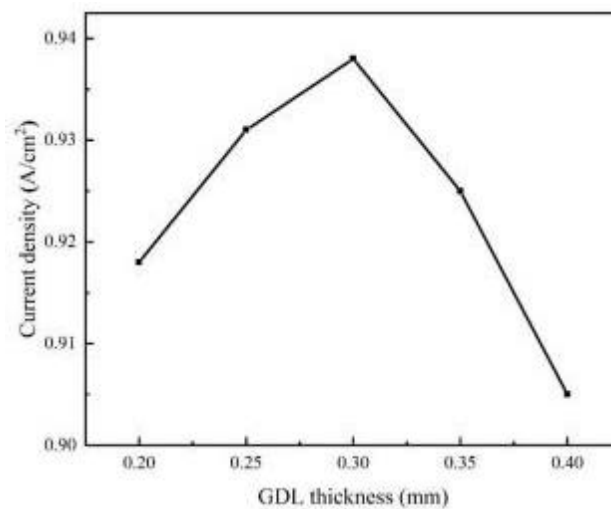


Figure 7. Thickness effects of performance.

4.2.2. Effect of porosity on performance

As shown in **Figure 8**, the results demonstrate that the performance of PEMFC is influenced by the porosity of both the GDL and the CL. Regarding the porosity of the GDL, as the porosity increases from 0.2 to 0.4, the performance gradually improves. A higher porosity facilitates faster and stronger diffusion of reactant gases within the GDL, enabling more reactants to reach the active sites. However, exceeding a certain point, further increasing the porosity of the GDL leads to a higher ohmic resistance, resulting in increased voltage drop or ohmic losses. This ohmic loss is directly proportional to the current density. However, after the porosity exceeds 0.4, there is a difference in the porosity behavior between the cathode and anode. Therefore, the cathode porosity continues to improve the cell performance after 0.4, while the anode porosity exhibits a decrease in performance. By studying the cathode and anode porosity separately and optimizing them, it is found that a cathode porosity of 0.48 and an anode porosity of 0.4 exhibit optimal performance. This is because there is the generation of liquid water on the cathode side, and timely drainage is beneficial for battery performance.

In terms of the porosity of the CL, as the anode CL porosity increases, the average current density of the PEMFC decreases, while as the cathode CL porosity increases, the current density increases. However, with the increase in CL porosity,

the conductivity of the catalytic layer decreases, and the catalyst loading decreases, which further reduces battery performance. Therefore, through optimization, the optimal cathode porosity of the catalytic layer is determined to be around 0.5, and the anode porosity is around 0.2. The primary reason for the notable porosity variation between the cathode and anode of the CL is the formation of liquid water on the cathode side. The porosity of the GDL and CL on the cathode and anode sides are interrelated, and their quantitative relationship can be effectively analyzed using neural networks. This underscores the importance of understanding and optimizing the porosity of the GDL and CL to maximize PEMFC performance. Through the analysis of parameters using the random forest algorithm, it was found that the importance proportion of the GDL porosity parameter reached 0.52, while the importance proportion of the GDL thickness was 0.31, accounting for almost 0.83 combined. In previous MEA studies, the thickness of the GDL and the cathode porosity were always considered as important parameters. This article further explains the reasons using RF. The importance of PEMFC features is shown in **Figure 9**.

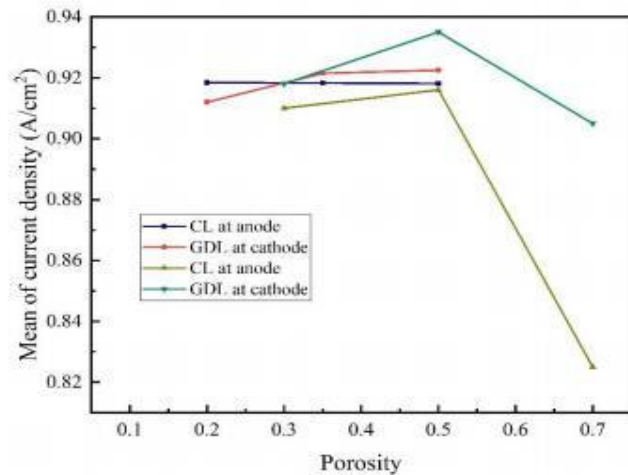


Figure 8. The effect of porosity of different structures on performance.

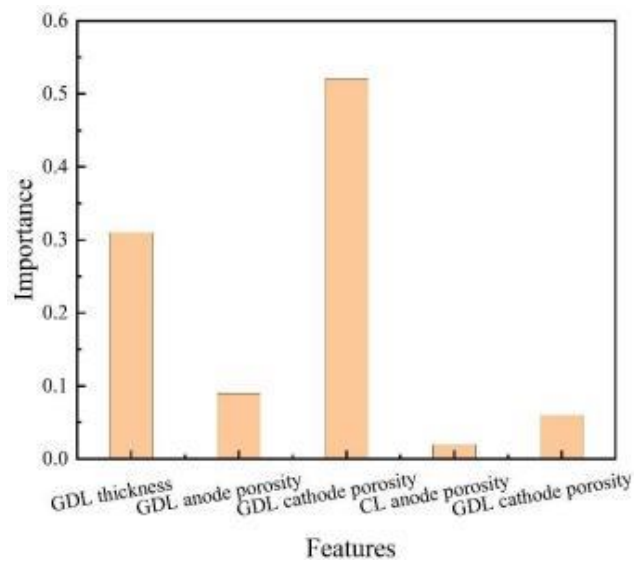


Figure 9. The importance of PEMFC features.

4.3. Parameter optimization results

Fast convergence is an important indicator for measuring an algorithm, by optimizing the ANN to build a surrogate model, it is possible to quickly find the optimal value [42]. In this study, algorithm improvements were made based on the characteristics of the ANN, further advancements have been made to enhance the speed quickly and accuracy of the algorithm. The convergence curve of the parameter optimization is depicted in the **Figure 10**. IDE has a significantly faster convergence speed compared to other algorithms. It is evident that the IDE algorithm exhibits excellent overall convergence, reaching a maximum current density of 0.9763 A/cm^2 at 30 iterations. Importantly, the IDE algorithm effectively prevents premature convergence and avoids getting stuck in local maxima. The **Table 7** presents the specific optimal parameters. To validate the reliability of the optimized framework, the maximum power of the optimized framework is compared with results from Computational Fluid Dynamics (CFD) calculations and data matching, the maximum errors for results are less than 6.0%. **Figure 11** illustrates a comparison of the polarization curve and power density curve for both the base model and the optimized model. Consequently, the optimized parameters are selected, leading to an 8.75% improvement in power density compared to the unoptimized parameters. Additionally, both oxygen distribution and current density distribution uniformity are enhanced, particularly in terms of improved oxygen distribution uniformity as shown in **Figures 12 and 13**.

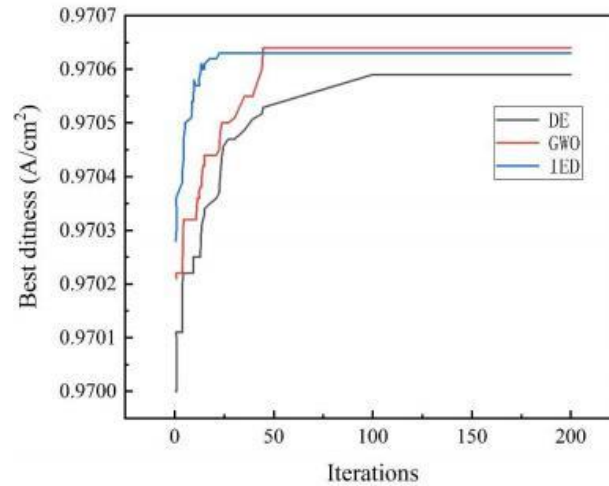


Figure 10. Convergence curve for parameter optimization.

Table 7. Comparison of parameters before and after optimization.

Parameters	Optimization value	Reference value
GDL thickness	0.228 mm	0.1 mm
GDL anode porosity	0.4	0.4
GDL cathode porosity	0.48	0.4
CL anode porosity	0.2	0.4
CL cathode porosity	0.5	0.4

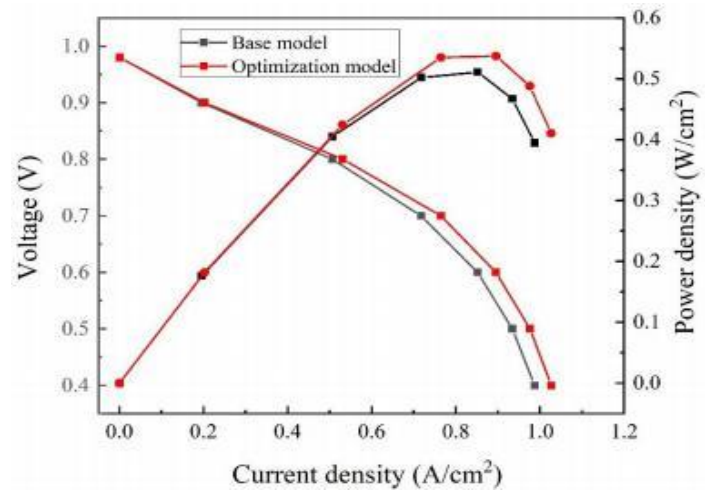


Figure 11. Polarization curves and net power density curves of the PEMFCs with base and optimization model.

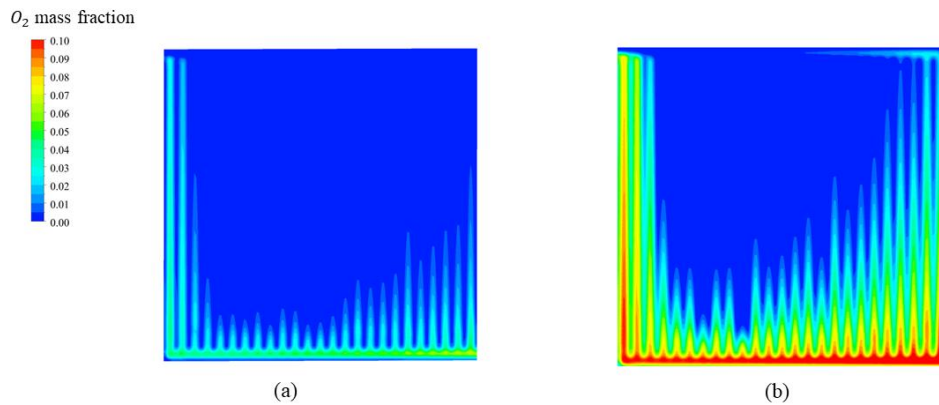


Figure 12. The O₂ distribution contours of (a) base model and (b) optimal model.

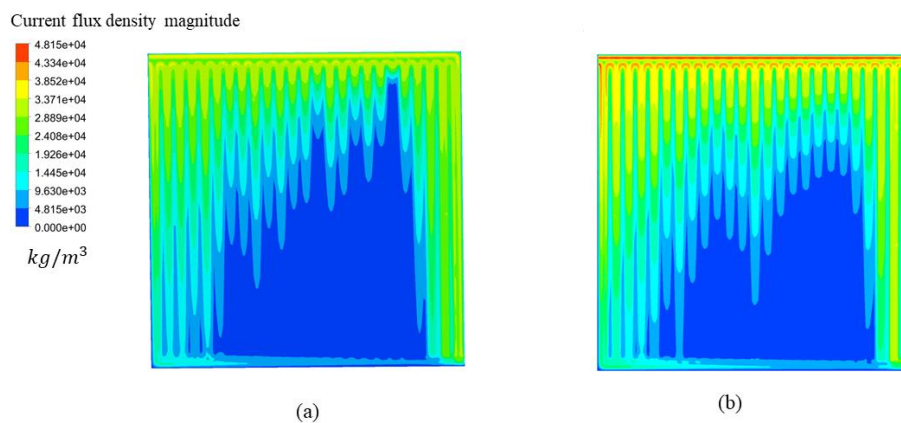


Figure 13. The current density distribution contours of (a) base model and (b) optimal model.

5. Summary

This research introduces a new method for forecasting PEMFC performance and optimizing its parameters through neural networks and an enhanced differential evolutionary algorithm. Initially, a 3D simulation model is created to serve as the

foundation for the optimization framework. Selected structural parameters are utilized as inputs for the neural network-based predictive model and as optimization variables for the improved differential evolution algorithm-driven framework. The goal of the optimization is to maximize power density. The findings indicate that the proposed method offers a valuable tool for predicting performance and optimizing parameters. Additionally, this optimization approach can be adapted for use in other energy systems to achieve efficient optimization. The key findings are summarized below:

(1) The Surrogate model is established through the ANN, in which the ANN adjusts the network structure by adjusting the weight and bias. Therefore, we improved the DE based on the network structure, combined with the greedy strategy in the optimization of DE, and introduced the evolution factor at the optimal value, which greatly accelerated the Rate of convergence speed and found the optimal solution faster.

(2) A novel framework is introduced for predicting PEMFC performance and optimizing its parameters, with focus on key factors like GDL thickness, GDL cathode porosity, and CL cathode porosity. The RF algorithm can calculate the importance of different feature parameters for battery performance and analyze the contribution of each parameter to battery performance. It can help us explain the “blank spot”:

(3) The data-driven model serves as a surrogate for the optimization framework. The findings reveal that the best-performing parameters are a GDL thickness of 0.228 mm, a GDL cathode porosity of 0.4 or 0.48, a CL cathode porosity of 0.2 or 0.5, leading to a maximum power density of 0.57 W/cm². This represents an 8.75% improvement over the unoptimized results. Furthermore, the maximum absolute discrepancy between the optimized framework and CFD results is 0.0013.

Author contributions: Conceptualization, TL and YL; methodology, YL; software, TL; validation, TL and YL; formal analysis, YL; investigation, TL; resources, YL; writing—original draft preparation, TL; writing—review and editing, TL; visualization, TL; supervision, YL. All authors have read and agreed to the published version of the manuscript.

Funding: This research was funded by the National Natural Science Foundation of China (grant number No. U2106226, 52305307) and foundation for Innovative Research Groups of the National Natural Science Foundation of China (grant number No. 52021003).

Ethical approval: Not applicable.

Conflict of interest: The authors declare no conflict of interest.

Nomenclature

s_m mass source term	σ_{eff} electron conductivity
s_v source term of momentum	ϕ electric potential
s_Q additional volumetric heat source term	ζ specific active surface area
c_k component concentration	γ concentration dependence
D_k^{eff} effective diffusion coefficient	α transfer coefficient

s_k component source term	η local surface overpotential
s_{ϕ_s} solid phase	σ_0 electron conductivity of a dense material
s_{ϕ_m} membrane phase	ε porosity
s volumetric transfer current	R resistance
$j_{a,ref}$ reference exchange current density	a anode
C concentration	BP bipolar plate
F Faraday constant	c cathode
ω electrolyte volume fraction	CH channel
	CL catalyst layer
	GDL gas diffusion layer

References

1. Y.D. Wang, Q. Meyer, K. Tang, J.E. McClure, R.T. White, S.T. Kelly, M.M. Crawford, F. Iacoviello, D.J.L. Brett, P.R. Shearing, P. Mostaghimi, C. Zhao, R.T. Armstrong, Large-scale physically accurate modelling of real proton exchange membrane fuel cell with deep learning, *Nat Commun*, 14 (2023) 745.
2. C. Lee, W.J.M. Kort-Kamp, H. Yu, D.A. Cullen, B.M. Patterson, T.A. Arman, S. Komini Babu, R. Mukundan, R.L. Borup, J.S. Spendelow, Grooved electrodes for high-power-density fuel cells, *Nature Energy*, (2023).
3. K. Jiao, J. Xuan, Q. Du, Z. Bao, B. Xie, B. Wang, Y. Zhao, L. Fan, H. Wang, Z. Hou, S. Huo, N.P. Brandon, Y. Yin, M.D. Guiver, Designing the next generation of proton-exchange membrane fuel cells, *Nature*, (2021).
4. A.C. Turkmen, C. Celik, The effect of different gas diffusion layer porosity on proton exchange membrane fuel cells, *Fuel*, (2018).
5. P. Yang, Y. Wang, Y. Yang, L. Yuan, Z. Jin, Effects of Gas Diffusion Layer Porosity Distribution on Proton Exchange Membrane Fuel Cell, *Energy Technology*, (2021).
6. B.W. Wang, B. Xie, J. Xuan, K. Jiao, AI-based optimization of PEM fuel cell catalyst layers for maximum power density via data-driven surrogate modeling, *Energy Conversion and Management*, 205 (2020).
7. H. Deng, Y. Hou, W. Chen, F. Pan, K. Jiao, Lattice Boltzmann simulation of oxygen diffusion and electrochemical reaction inside catalyst layer of PEM fuel cells, *International Journal of Heat and Mass Transfer*, 143 (2019).
8. S. Liu, C. Chen, J. Tan, H. Hu, D. Xuan, Multi-objective optimization of porous layers for proton exchange membrane fuel cells based on neural network surrogate model, *International Journal of Energy Research*, 46 (2022) 19796-19813.
9. H.-W. Li, B.-S. Xu, C.-H. Du, Y. Yang, Performance prediction and power density maximization of a proton exchange membrane fuel cell based on deep belief network, *Journal of Power Sources*, 461 (2020).
10. H.-W. Li, B.-X. Qiao, J.-N. Liu, Y. Yang, W. Fan, G.-L. Lu, A data-driven framework for performance prediction and parameter optimization of a proton exchange membrane fuel cell, *Energy Conversion and Management*, 271 (2022).
11. Turgut, M.T. Coban, Optimal proton exchange membrane fuel cell modelling based on hybrid Teaching Learning Based Optimization – Differential Evolution algorithm, *Ain Shams Engineering Journal*, (2015).
12. Huo W, Li W, Zhang Z, et al. Performance prediction of proton-exchange membrane fuel cell based on convolutional neural network and random forest feature selection. *Energy Conversion and Management*. 2021; 243: 114367.
13. P. Abraham B, K. Murugavel K, Influence of Catalyst Layer and Gas Diffusion Layer Porosity in Proton Exchange Membrane Fuel Cell Performance, *Electrochimica Acta*, (2021).
14. Y. Liu, S. Wu, Y. Qin, M. Zhang, X. Liu, J. Zhang, Y. Yin, Mass transport and performance of proton exchange membrane fuel cell considering the influence of porosity distribution of gas diffusion layer, *International Journal of Green Energy*, (2021).
15. G. Zhang, L. Wu, C. Tongsh, Z. Qu, S. Wu, B. Xie, W. Huo, Q. Du, H. Wang, L. An, N. Wang, J. Xuan, W. Chen, F. Xi, Z. Wang, K. Jiao, Structure Design for Ultrahigh Power Density Proton Exchange Membrane Fuel Cell, *Small Methods*, 7 (2023) e2201537.
16. W. Fan, T. Zhao, K. Jiang, L. Sun, S. Jia, Q. Wu, G. Lu, Z. Liu, Plant vs. Animal Prototype for Designing Bio-inspired PEMFC Flow Fields: Corn Veins or Murray's Law?, *Journal of Bionic Engineering*, (2022).

17. W. Yuan, Y. Tang, M. Pan, Z. Li, B. Tang, Model prediction of effects of operating parameters on proton exchange membrane fuel cell performance, *Renewable Energy*, (2010).
18. G. Zhang, B. Xie, Z. Bao, Z. Niu, K. Jiao, Multi-phase simulation of proton exchange membrane fuel cell with 3D fine mesh flow field, *International Journal of Energy Research*, (2018).
19. S. Um, C.Y. Wang, Three-dimensional analysis of transport and electrochemical reactions in polymer electrolyte fuel cells, *Journal of Power Sources*, (2004).
20. K.Y. Hu, P.Y. Zhao, S.X. Wang, Y.L. Wang, Three-dimensional multiphase simulation of a partially narrowed flow field configuration for a high-performance polymer electrolyte membrane fuel cell, *Applied Thermal Engineering*, 223 (2023).
21. N. Guo, M.C. Leu, U.O. Koylu, Bio-inspired flow field designs for polymer electrolyte membrane fuel cells, *International Journal of Hydrogen Energy*, (2014).
22. D. Lorenzini-Gutierrez, A. Hernandez-Guerrero, B. Ramos-Alvarado, I. Perez-Raya, A. Alatorre-Ordaz, Performance analysis of a proton exchange membrane fuel cell using tree-shaped designs for flow distribution, *International Journal of Hydrogen Energy*, (2013).
23. D. Mahmoud, Z. Xing, Enhancing reliability and lifespan of PEM fuel cells through neural network-based fault detection and classification, *International Journal of Hydrogen Energy*, (2023).
24. T. Wilberforce, A.G. Olabi, Proton exchange membrane fuel cell performance prediction using artificial neural network, *International Journal of Hydrogen Energy*, (2020).
25. C. Zhijie, Z. Wei, Z. Kun, L. Qingqing, H. Yuhan, E. Jiaqiang, Multi-objective optimization of proton exchange membrane fuel cells by RSM and NSGA-II, *Energy Conversion and Management*, (2023).
26. B. Yang, J. Wang, L. Yu, H. Shu, T. Yu, X. Zhang, W. Yao, L. Sun, A critical survey on proton exchange membrane fuel cell parameter estimation using meta-heuristic algorithms, *Journal of Cleaner Production*, 265 (2020).
27. C. Guo, J. Lu, Z. Tian, W. Guo, A. Darvishan, Optimization of critical parameters of PEM fuel cell using TLBO-DE based on Elman neural network, *Energy Conversion and Management*, (2019).
28. D. Runben, W. Xuezhe, W. Xueyuan, C. Siqi, Y. Hao, D. Haifeng, M. Pingwen, A fault diagnosis model for proton exchange membrane fuel cell based on impedance identification with differential evolution algorithm, *International Journal of Hydrogen Energy*, (2021).
29. W. Zhu, J.-a. Fang, W. Zhang, Y. Xu, L. Tong, A Hybrid Differential Evolution for Optimum Modeling of PEM Fuel Cells, *Arabian Journal for Science and Engineering*, (2014).
30. Fathy, M.A. Elaziz, A.G. Alharbi, A Novel Approach Based on Hybrid Vortex Search Algorithm and Differential Evolution for Identifying the Optimal Parameters of PEM Fuel Cell, *Renewable Energy*, (2020).
31. W. Gong, Z. Cai, Accelerating parameter identification of proton exchange membrane fuel cell model with ranking-based differential evolution, *Energy*, (2013).
32. H. Guo, Y. Li, J. Li, H. Sun, D. Wang, X. Chen, Differential evolution improved with self-adaptive control parameters based on simulated annealing, *Swarm and Evolutionary Computation*, (2014).
33. W. Tabbi, B. Mohammad, O. Abdelnasir, Power and Voltage Modelling of a Proton-Exchange Membrane Fuel Cell Using Artificial Neural Networks, *Energies*, (2022).
34. C. Youngtak, H. Gyuyeong, G. Dela Quarme, H. Sungwon, Artificial neural network-based model predictive control for optimal operating conditions in proton exchange membrane fuel cells, *Journal of Cleaner Production*, (2022).
35. S.V. Puranik, A. Keyhani, F. Khorrami, Neural Network Modeling of Proton Exchange Membrane Fuel Cell, *IEEE Transactions on Energy Conversion*, (2010).
36. H.-W. Li, J.-N. Liu, Y. Yang, G.-L. Lu, B.-X. Qiao, Coupling flow channel optimization and Bagging neural network to achieve performance prediction for proton exchange membrane fuel cells with varying imitated water-drop block channel, *International Journal of Hydrogen Energy*, (2022).
37. S. Feng, W. Huang, Z. Huang, Q. Jian, Optimization of maximum power density output for proton exchange membrane fuel cell based on a data-driven surrogate model, *Applied Energy*, (2022).
38. G. Zhang, L. Wu, K. Jiao, P. Tian, B. Wang, Y. Wang, Z. Liu, Optimization of porous media flow field for proton exchange membrane fuel cell using a data-driven surrogate model, *Energy Conversion and Management*, (2020).
39. R. Pang, C. Zhang, H. Dai, Y. Bai, D. Hao, J. Chen, B. Zhang, Intelligent health states recognition of fuel cell by cell voltage consistency under typical operating parameters, *Applied Energy*, 305 (2022).

40. L. Shengnan, T. Jiaqi, H. Haoqin, L. Chenlei, X. Dongji, Multi-objective optimization of proton exchange membrane fuel cell geometry and operating parameters based on three new performance evaluation indexes, *Energy Conversion and Management*, (2023).
41. M. Xuping, L. Shengnan, T. Jiaqi, H. Haoqin, L. Chenlei, X. Dongji, Multi-objective optimization of gradient porosity of gas diffusion layer and operation parameters in PEMFC based on recombination optimization compromise strategy, *International Journal of Hydrogen Energy*, (2023).
42. X. Guoping, Y. Zeting, X. Lei, W. Changjiang, J. Shaobo, Performance improvement of solid oxide fuel cells by combining three-dimensional CFD modeling, artificial neural network and genetic algorithm, *Energy Conversion and Management*, (2022).